Check for updates

Unraveling the electronic mechanisms of transition metal and fluorine co-doping for enhanced electrochemical performance in sodium lithium manganese oxide cathodes

Duong Trong Nhan, [a,b] Nguyen Vo Anh Duy,[c] Nguyen Chi Ben,[d]
Duy Khanh Nguyen, [a,b] Yohandys A. Zulueta, [e] Nguyen To Van,[f]
Viet Bac Thi Phung, [g] Nguyen Van Nghia,[h] Minh Tho Nguyen [i,j] and
Minh Triet Dang ⋆[d]

Enhancing the structural stability and electronic and electrochemical properties of sodium-ion cathode materials is essential for developing the next generation of sodium-ion batteries. In this study, we carry out first-principles calculations to assess the performance of P2-type sodium lithium manganese oxide (NLM) cathodes co-doped with transition metals X (X = Sc, Ti, V, Cr, Fe, Co, Ni, Cu, and Zn) and fluorine. Our findings reveal that among the investigated transition metals and fluorine, codoping cobalt and fluorine atoms helps mitigate Jahn−Teller distortions, thus stabilizing the NLM cathodes. The stability of this most promising cobalt−fluorine co-doped heterostructure is further validated by experimental X-ray diffraction patterns synthesized by the standard sol−gel method. Regarding electronic properties, the pristine NLM systems exhibit ferromagnetic metallic behavior. However, cobalt−fluorine co-doped systems display ferromagnetic semi-metallic characteristics, featuring a mix of free holes and electrons. The doped system shows a higher carrier density and lower activation energies, leading to improved transport properties compared to the undoped systems. These results highlight the significant role of co-doping cobalt and fluorine atoms in creating high-performance sodium-ion cathodes.

[a]Laboratory for Computational Physics, Institute for Computational Science and Artificial Intelligence, Van Lang University, Ho Chi Minh City, Vietnam.
E-mail: nhan.duongtrong@vlu.edu.vn
[b]Faculty of Mechanical, Electrical, and Computer Engineering, Van Lang School of Technology, Van Lang University, Ho Chi Minh City, Vietnam
[c]FPT University, Can Tho Campus, 600 Nguyen Van Cu Street, An Binh Ward, Can Tho City, Vietnam
[d]Can Tho University, 3/2 Street, Ninh Kieu Ward, Can Tho, Vietnam.
E-mail: dmtriet@ctu.edu.vn
[e]Departamento de Física, Facultad de Ciencias Naturales y Exactas, Universidad de Oriente, CP-90500, Santiago de Cuba, Cuba
[f]Faculty of Chemico-Physical Engineering, Le Quy Don Technical University, Hanoi, Vietnam
[g]Center for Environmental Intelligence and College of Engineering & Computer Science, VinUniversity, Hanoi 100000, Vietnam
[h]Open Training Institute, Hanoi Architectural University, Km10, Nguyen Trai Street, Hanoi, Vietnam
[i]Laboratory for Chemical Computation and Modeling, Institute for Computational Science and Artificial Intelligence, Van Lang University, Ho Chi Minh City, Vietnam
[j]Faculty of Applied Technology, Van Lang School of Technology, Van Lang University, Ho Chi Minh City, Vietnam

1. Introduction

Due to the growing demand for energy storage in portable electronic devices and electric vehicles, the advancement of rechargeable lithium-ion batteries (LIBs) has become profoundly remarkable.[1,2] Currently, LIBs dominate the energy storage market for electronic devices thanks to their high energy density and specific storage capabilities. Nevertheless, concerns regarding the scarcity of lithium resources have prompted the exploration of alternative rechargeable batteries. Sodium-ion batteries (SIBs) have thus emerged as potential substitutes for LIBs owing to their cost-effectiveness and ample resources.[3,4] Of the cathode materials for SIBs, layered sodium oxides (Na_xXO_2), where X stands for transition metals, have gained substantial attention due to their layered structure, which can accommodate larger Na ions. The oxides provide not only extensive diffusion pathways but also offer structural stability.[4] Sodium-layered oxides are typically categorized into two main groups: P-type (P2 and P3) and O-type (O2 and O3), where the numbers 2 and 3 denote the quantity of stacked transition metal layers in each unit cell.[5] Among these variants, P2 materials are especially appealing due to

their high structural stability and low energy diffusion barriers, which facilitate the transport of Na^+ ions.[6] Furthermore, among this class of materials, P2-type Na_xMnO_2, for instance, demonstrates excellent electrochemical performance and a high specific capacity (>200 mAh g^{-1}).[7] However, these materials suffer from strong coulombic repulsion between neighboring Na^+ ions, forming an ordered arrangement known as the Na^+/vacancy ordering. This arrangement results in the formation of intermediate phases that hinder Na^+ diffusion, significantly reducing electrochemical performance.[6] Specifically, P2-$Na_{0.6}MnO_2$ synthesized using the sol–gel method exhibits a specific capacity of 140 mAh g^{-1} at 0.1 C but retains only 53.6% after 9 cycles.[8] Similarly, P2-$Na_{0.7}MnO_2$ with a nanostructure has a capacity of up to 163 mAh g^{-1} but falls below 50% capacity after 50 cycles.[9] Such a drawback opens the opportunity to find ways to enhance the cycling performance of Na_xXO_2 cathode materials.

The enhancement of electrochemical performance in P2-type materials is a pivotal area in developing more efficient energy storage devices. Recent studies proposed a myriad of strategies for improving these materials' functionalities, such as surface modification,[10,11] doping with metal elements,[12–16] and the precise control of the materials' morphology[17] that stand out as particularly effective methods. Surface modification, achieved by applying a conductive layer, mitigates adverse reactions between the electrolyte and the active material. This approach can employ various conductive materials, including carbon,[18–20] conductive polymers,[21–23] or metal oxides such as ZrO_2,[23] and SiO_2.[24] Despite its benefits, the main challenge associated with surface modification is its reliance on sophisticated technology and the high energy input required throughout the material fabrication process. Conversely, doping with metallic elements emerged as a robust strategy to enrich the sodium content in P2-Na_xXO_2 compositions, effectively addressing sodium deficiency and Na^+/vacancy ordering issues. Jin *et al.* demonstrated that upon introducing lithium atoms into the transition-metal layer, these resulting P2-type layered oxides attain a faster Na diffusion and a lower diffusion barrier.[25] Furthermore, some successively synthesized P2-$Na_xLi_yMn_zO_t$ oxides yielded promising results, demonstrating high specific capacities and energy densities.[26] For instance, $Na_{0.6}[Li_{0.2}Mn_{0.8}]O_2$ exhibits an initial capacity of 247 mAh g^{-1} and an average voltage of 3.52 V, giving rise to an energy density of 878.2 Wh kg^{-1}.[26] Additionally, diversifying the cation in P2-Na_xXO_2 *via* doping is an effective strategy to enhance battery electrochemical performance.[27] A good example is the formation of $Na_{2/3}MnO_2$ with Co in P2-$Na_{2/3}[Mn_{0.8}Co_{0.2}]O_2$, which has a discharge capacity of 175 mAh g^{-1} at 1.5–4.6 V. It maintains a coulombic efficiency of 90% after 100 cycles.[28] More interestingly, co-doping cations and anions in layered materials based on transition metal oxides also provides promising electrochemical performance. For instance, the co-doped O3-$NaNi_{1/3}Fe_{1/3}Mn_{1/3}O_2$ with Mo/F,[29] the co-doped P2-$Na_{0.4}MnO_2$ with Al/F,[30] and the co-doped P2-$Na_{2/3}Ni_{1/3}Mn_{2/3}O_2$ with Al/F[31] possess excellent capacity retention with over 90% after 100

cycles. However, the inclusion of other ions to facilitate an increased ratio of active cations to total cations, leading to enhanced specific capacity, is still limited. In this context, we carry out a more comprehensive elucidation of codoping effects on the stability and electrochemical properties of sodium-ion batteries.

In this work, we employ first-principles calculations to investigate the stability, electronic, and transport properties of P2-type layered sodium lithium manganese oxide cathodes co-doped with transition metals (X = Sc, Ti, V, Cr, Fe, Co, Ni, Cu, Zn) and fluorine. Our results demonstrate that the (Co, F) co-doped cathode is the most stable among the investigated materials, based on optimal lattice parameters, formation energies, and phonon spectra. We validate this stability by comparing simulated and experimental X-ray diffraction patterns, with the latter synthesized using the standard sol–gel method. The electronic and electrochemical performance of (Co, F) doped cathodes is further evaluated through spin-splitting band structures, orbital-projected density of states, spatial charge distributions, activation energies, and diffusion coefficients. Our findings show that (Co, F) doping significantly reduces Jahn–Teller distortions while enhancing structural stability, storage capacity, electronic conductivity, and ion mobility. These results highlight the potential of (Co, F) co-doped cathodes for advancing sodium-ion battery technology.

2. Computational methods

In this study, all periodic DFT optimizations are performed using the M3GNet-UP-2022 machine learning (ML) potential, implemented in the Amsterdam Modeling Suite (AMS) package.[32,33] The M3GNet-UP-2022 potential set is trained *via* deep learning algorithms to achieve accuracy comparable to the generalized gradient approximation (GGA) with Perdew, Burke, and Ernzerhof (PBE) exchange–correlation functional.[34] Structural optimizations are carried out until the stress energy per atom is below 10^{-5} Ha $Å^{-1}$, and the energy difference between consecutive steps is less than 10^{-6} Ha.

The electronic properties of the investigated cathode materials are calculated using a double-zeta polarization (DZP) basis set, with core orbitals frozen during the self-consistent field (SCF) procedure. Spin-polarized DFT calculations are performed within the GGA framework.[35] To mitigate the self-interaction error in DFT-GGA, particularly for highly localized d orbitals of transition metals, the DFT+U correction is applied with the following Hubbard U parameters: U_{Mn} = 4.2 eV,[36] U_{Co} = 4.91 eV,[36] U_V = 3.0 eV,[37] U_{Sc} = 7.0 eV,[38] U_{Ti} = 3.0 eV,[39] U_{Cr} = 3.0 eV,[40] U_{Fe} = 6.8 eV,[41] U_{Ni} = 5.0 eV,[42] U_{Cu} = 3.0 eV,[43] U_{Zn} = 10.0 eV.[44]

The spatial charge density is computed using the Vienna *ab initio* simulation package (VASP)[45,46] to investigate the electronic doping mechanisms of the studied cathode materials. To ensure accuracy and reliability, a Monkhorst–Pack scheme[47] is employed for Brillouin zone integration with a dense 50 × 50 × 50 k-point grid. The exchange–correlation

functional is constructed consistently with simulations performed in the AMS package. A plane-wave energy cutoff of 520 eV is applied, and the self-consistent field (SCF) calculations are converged to a threshold of 10^{-5} eV per cell. Structural optimization is carried out until the Hellmann–Feynman forces on atoms are reduced to below 0.01 eV Å^{-1}, ensuring a well-relaxed configuration for further analysis. The nuclear magnetic resonance (NMR) shielding tensors are also obtained using VASP's perturbative NMR extension with a small perturbation step size of 10^{-3} to ensure accurate numerical evaluation of the magnetic susceptibility derivatives. The plane-wave basis cutoff energy was set to 600 eV, and the electronic self-consistent field was converged to 10^{-6} eV, providing a sufficiently large basis and tight convergence for reliable NMR chemical shifts.

3. Results and discussion

a. Structural characteristics

To construct the investigated cathode materials, we first create the monoclinic $Na_8Mn_{10}O_{20}$ structure.[48] Side- and top-view visualizations of the optimized P2-sodium manganese oxide structure ($Na_8Mn_{10}O_{20}$) are shown in Fig. 1(a and c), while its optimal Bravais lattice constants and unit cell volume are listed in Table 1. In the optimized $Na_8Mn_{10}O_{20}$ structure (NM), two key chemical bonds of Na–O and Mn–O are formed with bond lengths of $d_{Na-O} = 2.654$ and $d_{Mn-O} = 2.321$ Å, respectively (Table 1). The Na–O bond is longer than the Mn–O due to the larger Wigner–Seitz radius of Na (1.757 Å) compared to Mn (1.323 Å). Consequently, the longer Na–O bond results in a weaker bond strength relative to Mn–O.

Based on the optimized $Na_8Mn_{10}O_{20}$ structure in Fig. 1(a and c), we construct the Li-doped $Na_8Mn_9O_{20}$ configuration ($Na_8LiMn_9O_{20}$-NLM) by substituting a manganese atom with a lithium atom. The thermal stability of these systems is assessed *via* their formation energies (E_{form}) (eqn (S1), SI), where all ten possible configurations are evaluated to identify the most stable one. Thanks to the high symmetry of the supercell (Table S1, SI), the four lowest-energy sites are positions 2, 5, 7, and 10. Among them, the NLM configuration exhibits higher thermal stability than the NM configuration, as indicated by its lower formation energy ($E_{form} = -1.24$ eV *versus* -1.22 eV for NM). However, because formation energies alone are insufficient to determine the most stable configuration, we conduct phonon calculations to assess dynamical stability using the same settings as in the geometry optimization. In the phonon spectra, smaller imaginary frequencies indicate higher dynamical stability. As shown in Fig. S1, the configuration with Li at position 7 is the most stable, exhibiting negligible imaginary phonon frequencies. Consequently, the most stable NLM configuration, in side-view and top-view projections, is displayed in Fig. 1(b and d), respectively. Li doping introduces new Li–O bonds in $Na_8LiMn_9O_{20}$, with non-uniform bond lengths. The critical Li–O bond length is $d_{Li-O} = 2.206$ Å (Table 1). The variation in Li–O bond lengths leads to anisotropic changes in the Bravais lattice parameters compared to the pristine structure, with $a = 15.224$ Å, $b = 2.958$ Å, and $c = 11.100$ Å. Thus, the unit cell volume contracts to $V = 436.822$ Å^3, consistent with previous reports.[49] Furthermore, the presence of Li–O bonds reduces the Na–O and Mn–O bond lengths, with $d_{Na-O} = 2.594$ Å and $d_{Mn-O} = 2.297$ Å (Table 1). This reduction occurs because d_{Li-O} is shorter than d_{Na-O} and d_{Mn-O}, causing localized structural distortions around the Li doping site.

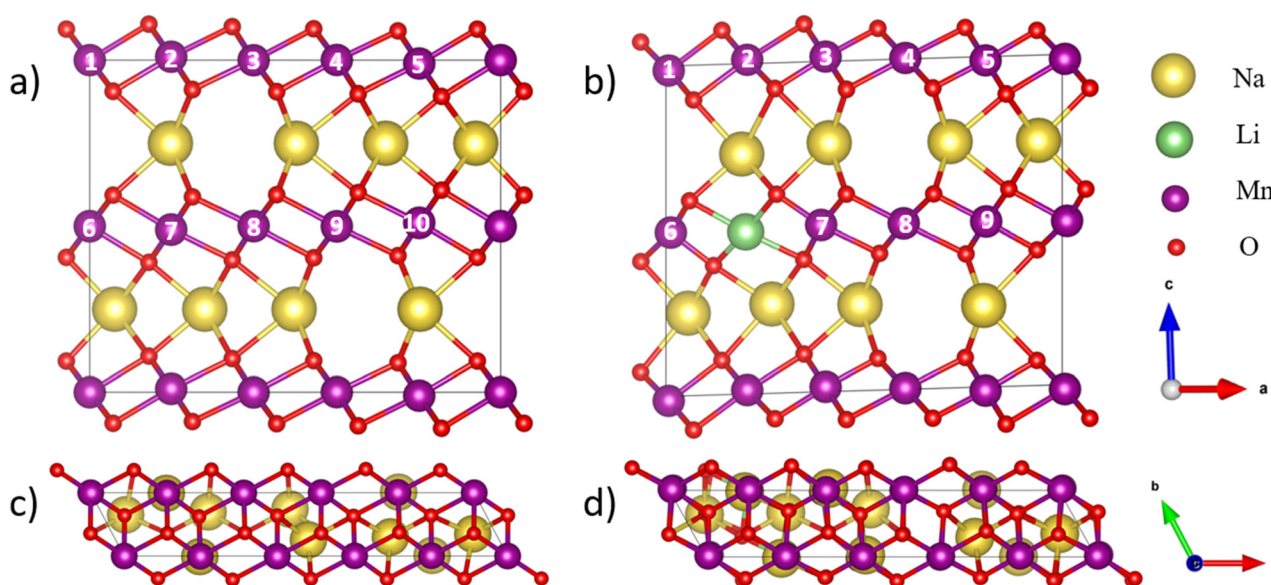**Fig. 1** Top-view and side-view of the optimized geometries of (a and c) $Na_8Mn_{10}O_{20}$ and (b and d) $Na_8LiMn_9O_{20}$. Yellow, green, purple, and red spheres represent Na, Li, Mn, and O atoms, respectively. Possible Li doping sites are labeled from 1 to 10.

Table 1 The Bravais lattice parameter (a, b, c), unit cell volume (V), average bond length (d), and formation energy (E_{form}) of the optimal $Na_8Mn_{10}O_{20}$ and $Na_8LiMn_9O_{20}$ configurations

Configuration	a (Å)	b (Å)	c (Å)	V (Å)	d_{Na-O} (Å)	d_{Mn-O} (Å)	d_{Li-O} (Å)	E_{form} (eV)
$Na_8Mn_{10}O_{20}$	15.588	2.913	11.120	446.466	2.440	2.069	X	−1.217
$Na_8LiMn_9O_{20}$	15.224	2.958	11.100	436.822	2.435	2.028	2.171	−1.244

Next, transition metal atoms (X = Sc, Ti, V, Cr, Fe, Co, Ni, Cu, Zn) are doped into the optimized NLM configuration by substituting a single Mn atom at one of the remaining nine Mn positions, see the numbered Mn atoms in Fig. 1(b and d). The resulting X-doped NLM configurations are analyzed based on their formation energies, calculated using eqn (S2). Among all possible configurations, the most energetically favorable structure is identified, with its optimized side-view and top-view geometries shown in Fig. 2(a and c), respectively. The X dopant atom is highlighted by a blue sphere. In cases where the formation energy alone is insufficient to determine the most stable configuration, such as for Co-doped NLM, as shown in Table S2, we further evaluate phonon spectra to assess dynamical stability. The 4th Co doping position is identified as the most energetically favorable configuration due to the presence of fewer imaginary modes (Fig. S2). X doping induces significant geometric modifications in the NLM structure, primarily due to the formation of new X–O chemical bonds, as detailed in Table 2. Notably, the Co-doped NLM configuration exhibits Bravais lattice parameters of a = 15.101 Å, b = 2.956 Å, c = 11.114 Å, and a unit cell volume of V = 432.564 Å^3. These values indicate minimal Jahn–Teller distortion, which is further confirmed by its partial distribution functions in Fig. S3. A smaller Jahn–Teller distortion implies greater structural stability during the charge/discharge cycle, making Co-doped NLM a promising candidate for battery applications.

To further enhance the stability of X-doped NLM cathode materials, we systematically investigate F co-doping, as fluorine has been recognized to improve specific capacity and enhance long-term structural stability of these configurations.[50–52] The (X, F) co-doped NLM structures are constructed by substituting a single O atom at the bottom O layer with an F atom. The optimized side-view and top-view geometries of these (X, F) co-doped NLM configurations are shown in Fig. 2(b and d), where the substituted F atom is marked in gray. F co-doping expands the unit cell volume, as seen in the Co-doped NLM configuration, where V increases from 432.564 Å^3 to 438.013 Å^3 upon (Co, F) co-doping (Table 2). This volume expansion improves sodium-ion storage capacity, proving that F co-doping enhances specific capacity and structural stability without distorting the critical geometries. Furthermore, we compute the formation energies of both X-doped NLM and (X, F) co-doped NLM configurations using eqn (S3), with results summarized in Table 2. The data confirm that F co-doping stabilizes the cathode materials, making them more energetically favorable than their non-F-doped counterparts.
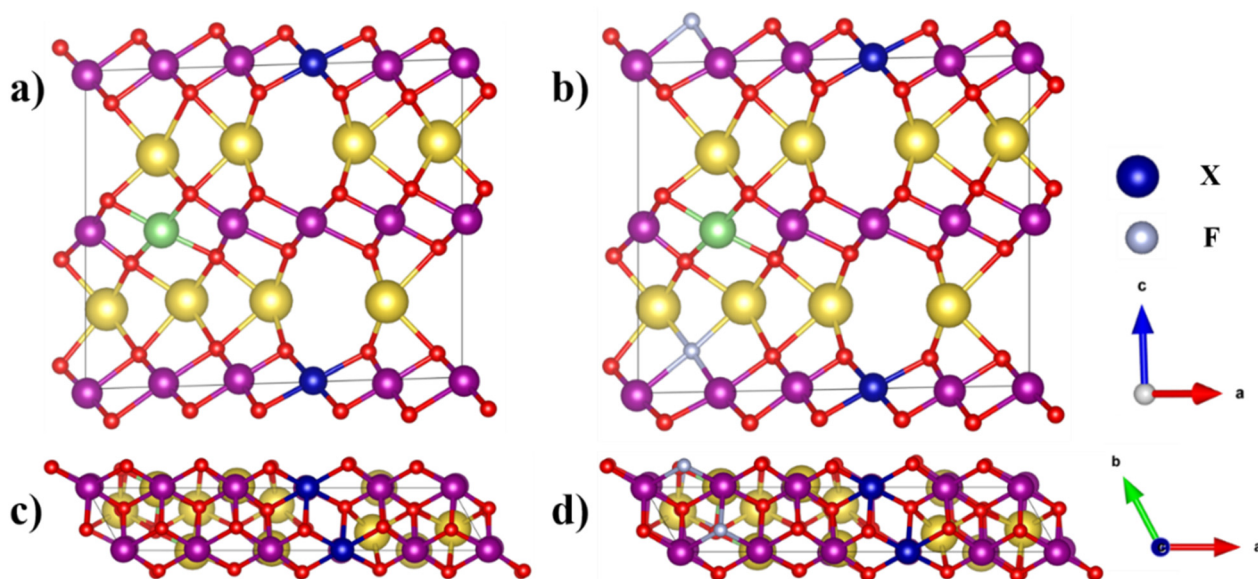

Fig. 2 Top-view and side-view of the optimized geometrical structures of (a and c) X-doped NLM ($Na_8LiMn_8XO_{20}$) and (b and d) (X, F) co-doped NLM ($Na_8LiMn_8XO_{19}F$). The blue and gray spheres represent transition metal atoms X (X = Sc, Ti, V, Cr, Fe, Co, Ni, Cu, and Zn) and F atoms, respectively.

Table 2 Bravias lattices (*a*, *b*, *c*), volume (*V*), average bond lengths, and formation energy (E_{form}) of X-doped and (X, F) co-doped NLM configurations

System	Sc	Ti	V	Cr	Fe	Co	Ni	Cu	Zn
a (Å)	15.208	15.260	15.214	15.112	15.129	15.101	15.058	15.152	15.145
b (Å)	2.985	2.950	2.944	2.968	2.970	2.956	2.952	2.947	2.954
c (Å)	11.107	11.095	11.097	11.105	11.114	11.114	11.105	11.094	11.091
V (Å^3)	439.235	437.190	435.550	433.713	434.990	432.564	430.156	432.587	432.998
d_{TM-O} (Å)	2.116	2.003	1.985	2.041	2.065	2.093	2.098	2.114	2.140
E_{form} (eV)	−1.415	−1.413	−1.289	−1.260	−1.205	−1.195	−1.164	−1.216	−1.262

System	Sc–F	Ti–F	V–F	Cr–F	Fe–F	Co–F	Ni–F	Cu–F	Zn–F
a (Å)	15.267	15.327	15.277	15.166	15.186	15.150	15.120	15.167	15.205
b (Å)	3.009	2.976	2.970	2.992	2.995	2.983	2.978	2.977	2.981
c (Å)	11.125	11.128	11.127	11.123	11.131	11.137	11.126	11.121	11.111
V (Å^3)	444.779	443.538	441.760	438.987	440.362	438.013	435.948	437.474	438.833
d_{TM-O}	2.116	2.008	1.990	2.040	2.065	2.087	2.098	2.092	2.138
d_{F-Mn}	2.303	2.324	2.327	2.306	2.304	2.305	2.301	2.304	2.290
d_{F-Na}	2.402	2.381	2.375	2.395	2.397	2.391	2.390	2.389	2.401
E_{form} (eV)	−1.454	−1.452	−1.328	−1.300	−1.244	−1.234	−1.203	−1.255	−1.301

The charging/discharging processes of Na ions (Na$^+$) strongly influence the structural stability of the electrodes. Greater interlayer spacing facilitates ion transport, improving charging/discharging efficiency.[53] To assess structural changes induced by F doping, we analyze the Mn–O bond lengths before and after F incorporation using pair distribution functions (PDFs) of Mn–O distances, as shown in Fig. S3(a–i). The red curves correspond to X-doped (X = Sc, V, Ti, Cr, Fe, Co, Ni, Cu, Zn) NLM configurations, while the blue curves represent (X, F)-co-doped NLMXF configurations. The PDF spectra of X-doped configurations (red curves) reveal three distinct Mn–O bond lengths (except for (Co, F) co-doped NLM, which exhibits only two). The highest peak appears at ~1.94 Å for all X-doped structures. Among them, (Co, F) co-doped NLM displays the lowest peak intensity (Fig. S3f). The presence of secondary peaks in the PDF spectra indicates Jahn–Teller distortions, which occur when specific metal centers within an octahedral configuration undergo asymmetric bond elongation along one axis while compressing along others. These distortions can contribute to structural degradation during cycling, leading to anisotropic lattice parameter changes.[54] Notably, our (Co, F) co-doped NLM exhibits a negligible secondary Mn–O peak, confirming the suppression of Jahn–Teller distortions and enhanced structural integrity. This agrees with prior reports on multi-cation disordering in K-ion layered oxides, where shorter and stronger TM–O bonds were found to maintain stability during cycling.[55] Furthermore, similar to the coherent spinel-layered structures observed in fluorinated Li- and Mn-rich oxides,[56] (Co, F) co-doping in our system expands the lattice volume while stabilizing the framework, thereby facilitating Na$^+$ transport without sacrificing stability.

Most essentially, the (Co, F) co-doped NLM configuration exhibits a negligible second peak, while other X-doped structures show more pronounced secondary peaks. This confirms that Co doping minimizes Jahn–Teller distortions, enhancing structural integrity. Furthermore, after F co-doping (blue curves, Fig. S3), the full width at half maximum (FWHM) of the PDF peaks expands toward larger distances, indicating an increase in unit cell volume (see Table 2). This expansion suggests that F co-doping facilitates Na$^+$ ion diffusion, improving electrochemical performance. Additionally, F doping reduces the density of secondary peaks in the PDF spectra, signifying weaker Jahn–Teller distortions. In particular, (Co, F) co-doped NLM further suppresses the secondary peak, indicating that (Co, F) co-doping effectively mitigates structural distortions caused by the Jahn–Teller effect. This structural reinforcement enhances long-term stability. Among all (X, F) co-doped NLM configurations, the (Co, F) co-doped NLM emerges as the most promising cathode material for sodium-ion batteries, offering superior structural stability and improved ion transport.

To further evaluate the stability of the most stable structures predicted by DFT simulations, we employ the standard sol–gel method, which is commonly used to achieve a homogeneous material composition at the molecular level. We synthesize the (Co–F) co-doped NLM cathode materials step-by-step, following a procedure similar to that presented previously. The synthesis involves dissolving precursor salts in a citric acid solution, followed by controlled heating to form an aerogel. This aerogel was subsequently calcined at high temperatures to produce the final crystalline material. For details of the synthesis, we refer to ref. 52 and Table S3. Fig. S4 and Table S4 compare DFT-simulated and experimental X-ray diffraction (XRD) data for NLM and its doped variants (Co-doped NLM, F-doped NLM, and (Co, F) co-doped NLM). Table S4 reveals a strong correlation, with most peak deviations within 3%. The (Co, F) co-doped NLM sample exhibits the best agreement, indicating enhanced structural stability and minimal distortion from doping. The primary discrepancies, observed in peaks (102) and (103), are likely due to doping-induced lattice distortions. Despite minor variations, the overall phase consistency and trends in lattice parameters confirm the

reliability of DFT in predicting material structures. These findings highlight the significant role of (Co, F) co-doping in reinforcing the structural stability of NLM cathodes.

b. Electronic properties

In this section, using DFT+U calculations, we investigate the electronic band structures for NM, NLM, X-doped NLM, and (X, F) co-doped NLM systems. The first Brillouin zone scheme, with specific band paths $A_1 \rightarrow G \rightarrow A_2$, $A_6 \rightarrow G \rightarrow A_5$, $A_3 \rightarrow G \rightarrow A_4$, $G \rightarrow A_7$ highlighted in red, is presented in Fig. S5. The Fermi level (E_F) is set to zero, distinguishing the valence and conduction states, as indicated by the solid black lines. In Fig. S6(a), the pristine NM system exhibits spin-splitting energy bands, represented by solid red lines (spin-up states) and dotted blue lines (spin-down states). This spin-splitting is more pronounced at low-lying energies near the Fermi level and in the higher conduction band, whereas spin degeneracy appears at deep valence energies below -1.5 eV. The presence of spin-splitting energy bands indicates a ferromagnetic character in the NM systems.

Two distinct types of energy dispersion are identified: saddle-like dispersion at low-lying and higher energies and parabolic dispersion at deep valence energies. At the Fermi level, several highest spin-up valence bands intersect E_F, generating free electrons, which characterize the system as an n-type metal. This n-type conductivity indicates good electronic conductivity, making the material suitable for electrode applications. The outermost valence orbitals predominantly govern the electronic properties, as demonstrated by the d-orbital-contributed electronic band structure in Fig. 3(a). Here, solid magenta and dotted green lines represent spin-up and spin-down states, respectively. The primary features of Fig. S6(a) closely resemble those of Fig. 3(a), reinforcing the role of d orbitals in defining the electronic characteristics of the system. The representation of the Fermi level, spin states, and pristine band structures remains consistent across all doped systems. Upon Li doping (NLM), the electronic structure, including spin-splitting bands and energy dispersions, remains largely unchanged compared to the pristine system (Fig. S6(b) and Fig. 3(b)). However, the highest spin-up valence bands shift upward due to the transfer of Li's valence electrons to the host, increasing free electron availability and thereby enhancing electronic conductivity. In contrast, Co doping in the Co-doped system significantly alters the electronic band structures (Fig. S6(c) and Fig. 3(c)). The increased spin-splitting near E_F enhances the system's ferromagnetic properties, enabling the simultaneous generation of free electrons and holes and leading to semi-metallic behavior, as later confirmed by charge distribution analysis. These modifications stem from the dominant role of d-orbitals, which is consistent with observations in pristine systems. Furthermore, F co-doping alongside Co introduces changes to the electronic band structures, extending spin-splitting across the entire energy range (Fig. S6(d) and Fig. 3(d)). This co-doping enhances both ferrimagnetic behavior and electronic conductivity due to the combined contribution of spin-up and spin-down electrons and

spin-up holes. As a result, the (Co, F)-co-doped NLM system emerges as a highly conductive cathode material, offering superior electronic performance and an increased net free carrier concentration. The increased carrier density observed in the (Co, F) co-doped system is consistent with recent fluorination studies in Li-rich cathodes, where a surface-to-bulk Mn^{3+} gradient improved conductivity and mitigated voltage decay.[56] Moreover, the role of anion–cation co-doping in tuning electronic structure has been demonstrated for Al^{3+}/PO_4^{3-} co-doped LMR materials, which showed enhanced oxygen-vacancy concentration and improved Li^+ mobility.[57] These parallels reinforce that (Co, F) co-doping effectively balances orbital occupations, suppresses Jahn–Teller active states, and promotes high conductivity for NLM cathode materials.

We analyze the orbital-projected density of states (PDOS) for the considered systems to validate the key features observed in the electronic band structures. The PDOS of the Co-doped system is shown in Fig. 4, while those of other X-doped configurations are presented in Fig. S7 and S8. Again, the Fermi level is set to zero energy, distinguishing the valence and conduction states, as indicated by the dashed black line. The gray, red, and blue regions correspond to contributions from s, p, and d orbitals, respectively. Positive and negative DOS values represent spin-up and spin-down states, and the asymmetry between these peaks indicates the presence of spin-splitting bands and a ferromagnetic character. In the pristine NM system, spin-up states at E_F arise from spin-up bands intersecting the Fermi level, leading to n-type metallic behavior (Fig. 4a). The prominent asymmetric peaks around E_F are a direct consequence of spin splitting, providing strong evidence of ferromagnetic properties. Regarding orbital contributions, p orbitals exhibit the highest electron density. In contrast, Mn d orbitals ($[Ar]3d^5 4s^2$) contribute more to the PDOS than s orbitals, which play a minimal role across the energy spectrum. Upon Li doping, the PDOS undergoes noticeable modifications (Fig. 4b). Specifically, the spin-up states at the Fermi level shift to higher energies, increasing free electron concentration and thereby enhancing electronic conductivity. This shift aligns with the upward movement of the highest spin-up valence bands in the corresponding electronic band structure.

A significant modification in the PDOS is observed in the d-orbital contributions. In the spin-down states at the highest conduction energy of Fig. 4a, a single peak splits into two prominent peaks in Fig. 4b. With Co doping, the PDOS undergoes substantial reshaping in Fig. 4c, where the states at the Fermi level expand due to the upward shift of the spin-up highest valence bands and the downward shift of the lowest conduction bands. This modification increases free carriers by facilitating the simultaneous generation of electrons and holes, significantly enhancing electronic conductivity compared to the NLM system. In the Co-doped systems, the five d orbitals of the transition metal split into two distinct groups under an octahedral arrangement: the higher-energy (e_g) orbitals (d_{z^2} and $d_{x^2-y^2}$) and the lower-energy t_{2g} orbitals (d_{xz}, d_{yz}, and d_{xy}).[58] Electrons occupying the e_g states often induce Jahn–Teller distortions, which can impede Na^+ transport during the
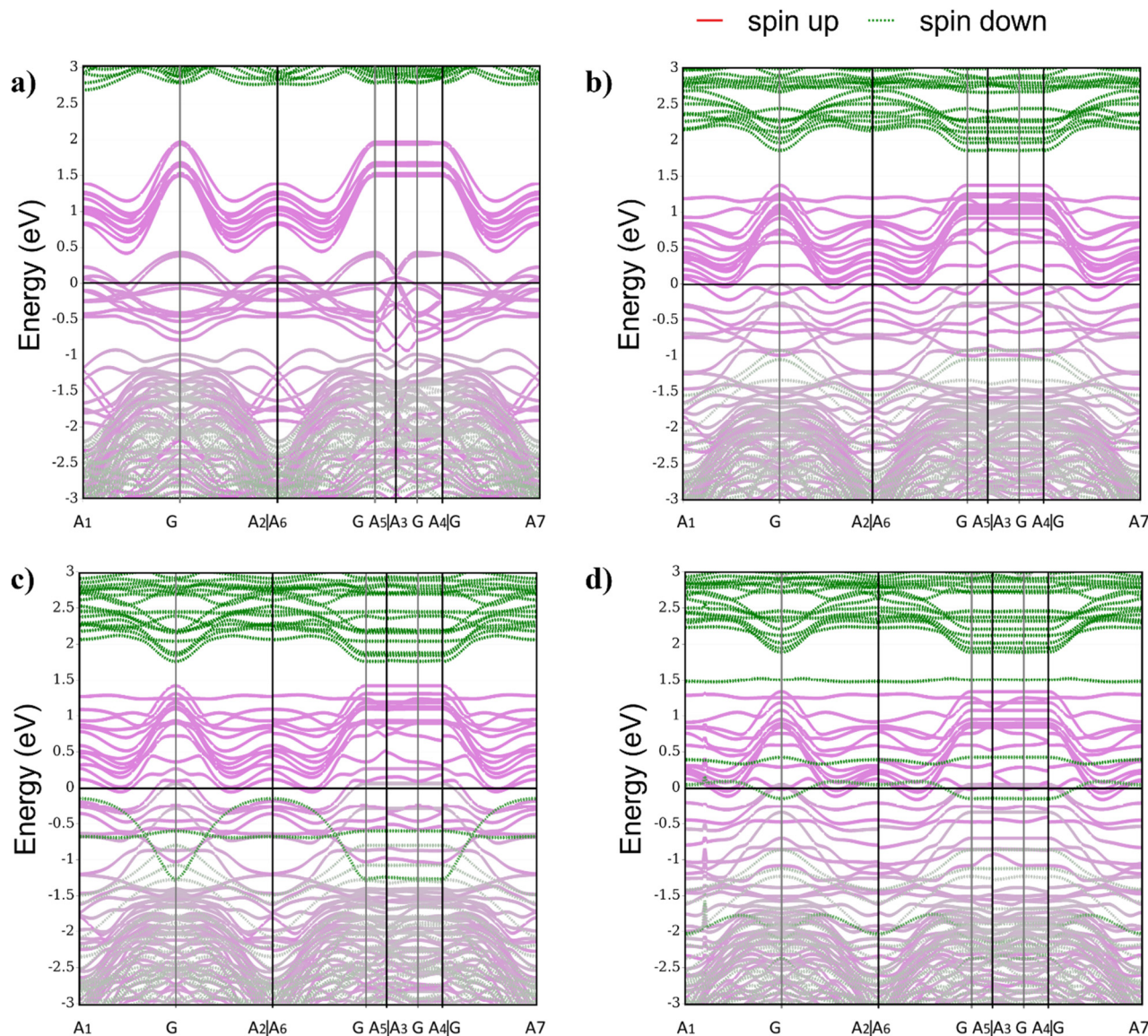
— spin up   ···· spin down

Fig. 3 The d-orbital electronic band structures of (a) NM, (b) NLM, (c) Co-doped NLM, and (d) (Co, F) co-doped NLM.

charging/discharging process. To assess this effect, we analyze the PDOS contributions of e_g and t_{2g} energy levels in the Co-doped NLM system, revealing an overlap between these levels. Upon F doping, the PDOS of the (Co, F)-co-doped NLM system (Fig. 4d) shows an extension of spin-up states into lower energy regions, confirming the intersection of the spin-down lowest conduction band and spin-up highest valence band at the Fermi level. This intersection substantially increases free carrier concentration, further enhancing electronic conductivity. Additionally, F doping elevates the energy density of the Co t_{2g} orbitals, leading to dominance of t_{2g} states at the Fermi level. Among all investigated systems, the $Na_8LiMn_8CoO_{19}F$ configuration exhibits the highest t_{2g} density, minimizing Jahn–Teller distortions by limiting available doping sites. This stabilization highlights (Co, F) co-doping as a promising strategy for cathode applications.

Spatial charge density distribution provides crucial insights into charge transfer mechanisms induced by dopant atoms. This distribution helps explain Fermi level shifts in n-type and p-type doped systems, affecting the highest valence and lowest conduction bands, thereby modulating electronic conductivity. Additionally, doping extends states at the Fermi level into lower energy ranges in the density of states (DOS). Using DFT+U calculations implemented in the VASP package, we analyze the spatial charge distributions of NLM, Co-doped NLM, and (Co, F) co-doped NLM systems, as shown in Fig. 5. In these figures, the yellow isosurface/red regions represent charge accumulation (acceptor sites). In contrast, the vacant isosurface corresponds to charge depletion (donor sites). To better visualize the charge behavior of dopant atoms, they are marked with black circles in Fig. 5. In the Li-doped NM system (Fig. 5a), the Li adatom (green sphere, black circle) introduces
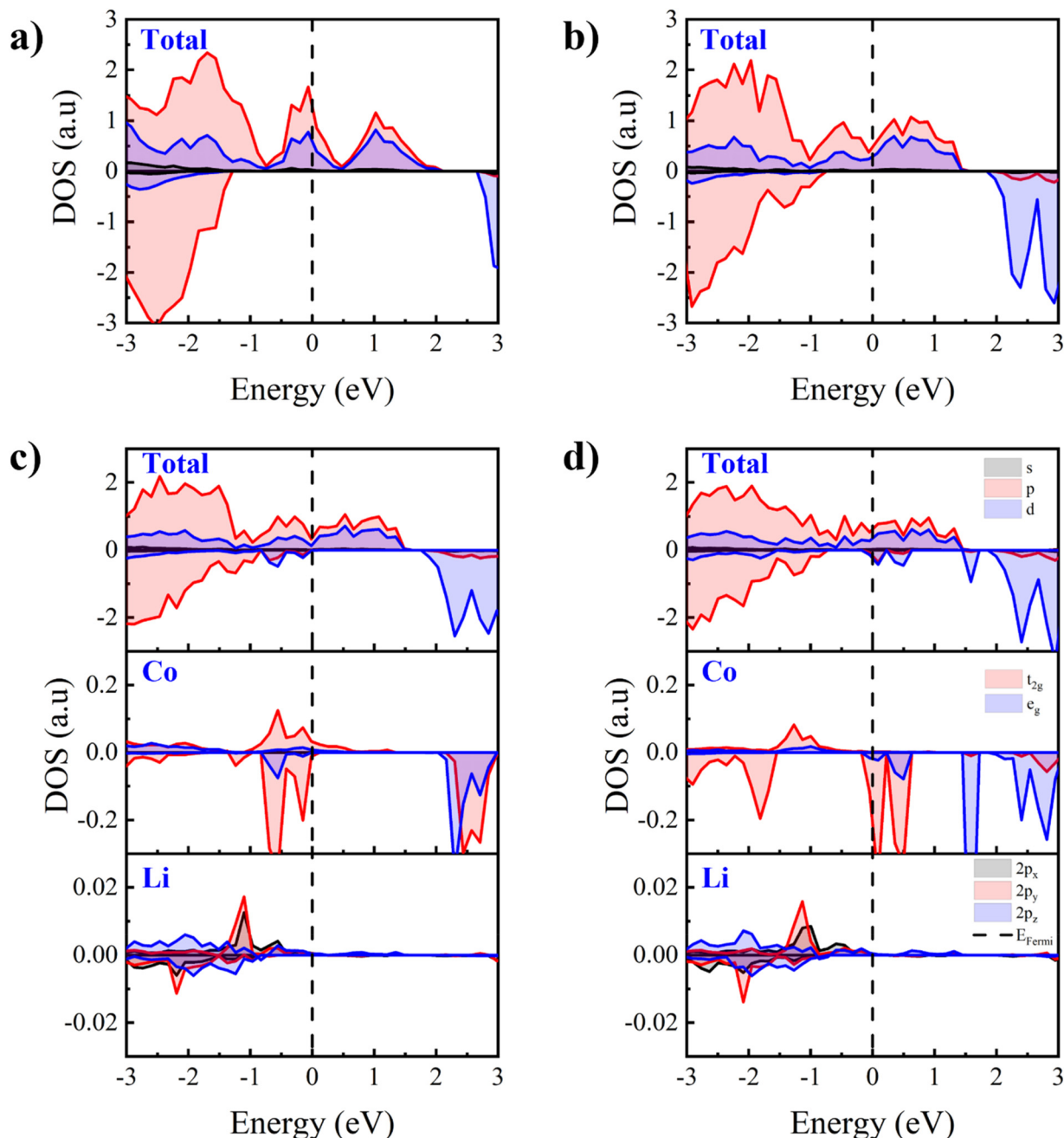
Fig. 4 PDOS calculated by the DFT+U method of (a) NM, (b) NLM, (c) Co-doped NLM, and (d) (Co, F)-co-doped NLM systems.

localized charge redistribution around the doped site. Li donates its outermost valence electrons to neighboring host atoms, becoming a donor, as evidenced by the charge depletion region surrounding it. In contrast, neighboring host atoms act as acceptors. This charge loss behavior results in a higher shift of the highest valence bands intersecting the Fermi level, thereby increasing the availability of free electrons. A key advantage of Li doping is its ability to enhance electronic conductivity by extending states at the Fermi level, as confirmed by both electronic band structure and PDOS analysis.

Thus, this donor charge behavior facilitates electron and ion transport, reinforcing its potential for electrode applications.

The introduction of Co co-doping in the NLM system significantly modifies the charge density distribution, as shown in Fig. 5b, where the Co adatom (blue sphere) is prominently marked. Co doping induces localized charge separation, creating distinct charge redistribution regions around its doping site (black circle). Specifically, Co acts as an electron acceptor, attracting electrons from its neighboring atoms. This acceptor behavior, coupled with the remaining Li donor, facilitates the
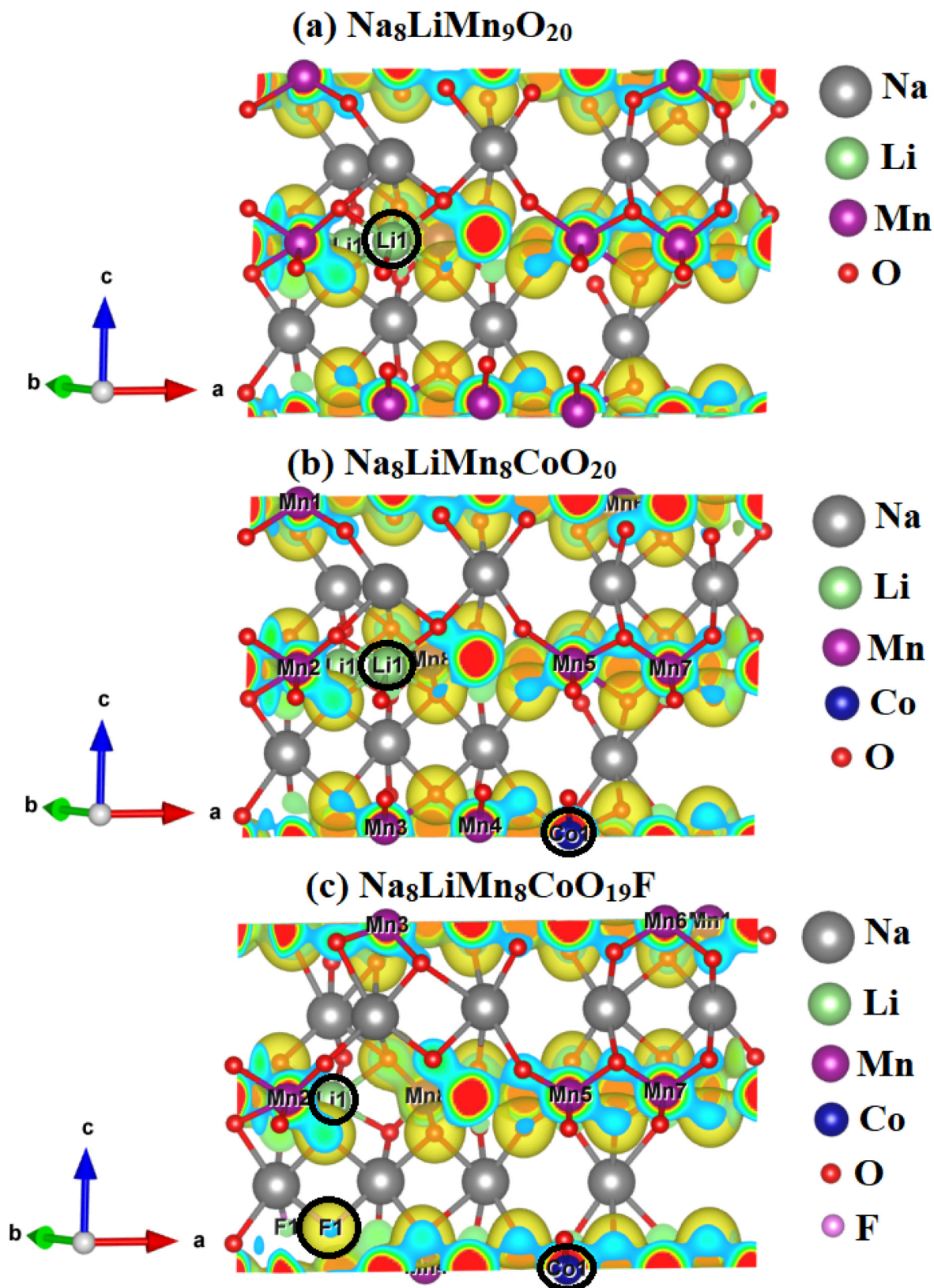
Fig. 5 Spatial charge density distributions of (a) NLM, (b) Co-doped NLM, and (c) (Co, F) co-doped NLM systems. The yellow iso-surface displays the charge accumulation, and the vacant iso-surface illustrates the charge depletion. Black circles mark the doped atoms.

coexistence of electrons and holes, effectively increasing the free carrier concentration and enhancing electronic conductivity. This charge redistribution mechanism reinforces the suitability of Co co-doped NLM as a cathode material for sodium-ion batteries.

Upon (Co, F) co-doping in the NLM system, the charge density distribution becomes even more intricate, as illustrated in Fig. 5c. The F adatom (gray sphere), acting as an additional electron acceptor, further intensifies charge separation within the system. The combined effect of the Co acceptor, F acceptor, and Li donor significantly boosts the free carrier density, leading to a substantial enhancement in electronic conductivity. The (Co, F) co-doped NLM system exhibits the highest electronic conductivity, positioning it as the most promising cathode material among other investigated configurations.

These findings are further reinforced by the combined Bader charge and ^{19}F nuclear magnetic resonance (NMR) analyses, which provide a consistent picture of how (Co, F) co-doping enhances the electronic performance of NLM cathodes. Charge redistribution maps (Fig. S9) reveal that Co substitution acts as a strong electron acceptor ($\Delta\rho \sim -1e$), promoting cationic redox activity, while the addition of F intensifies local charge separation, particularly at Mn sites adjacent to Li, where $\Delta\rho$ exceeds $+3e$. This pronounced charge gradient enhances Mn–O bond polarization, suppresses Jahn–Teller distortions, and facilitates greater electronic delocalization. Complementarily, the ^{19}F NMR chemical shifts (Table S5) show highly negative isotropic chemical shifts ($\delta_{iso} \approx -856$ to -900 ppm) for F-containing systems, reflecting strong shielding effects from Co–F bonding and significant electronic redistribution around F sites. The large anisotropy ($\delta_{csa} \approx 190$–490 ppm) confirms that fluorine atoms occupy highly anisotropic bonding environments, strengthening directional

bonding interactions. Taken together, these results demonstrate that the cooperative effect of Co and F not only stabilizes the transition-metal–oxygen framework but also maximizes free carrier density and conductivity, thereby providing a clear pathway to improved structural stability and superior electronic performance.

c. Transport properties

High ion diffusivity and electronic conductivity are requirements for cathode materials used in the ultrafast charging capabilities of SIBs.[59,60] This combination ensures the battery can quickly absorb and release energy without significant degradation. Optimizing these properties helps achieve higher energy densities, thereby enhancing the performance, longevity, and efficiency of SIBs.[59–61] This makes them more viable for a wide range of applications, from portable electronics to large-scale energy storage.[59–61]

The Arrhenius dependence of the conductivity and diffusivity of NLM, Co-doped NLM, and (Co, F) co-doped NLM systems in the temperature range of 250–550 K are shown in Fig. 6, respectively. The conductivity data are obtained using the Nernst–Einstein equation, where the diffusion coefficient at each temperature is directly related to the conductivity of Na$^+$ ions.[62–64] We refer to part 4 in the SI for details of these calculations. Table 3 presents the predicted activation energy for the diffusion (E_a^D) and the direct current (DC) conductivity (E_a^σ), including the conductivity (σ_0) and diffusion coefficient (D_0) of each compound at room temperature. Effective jumps in mass transport contribute to the charge transport process, thereby reducing the conduction activation energy. As shown in Table 3, doping cobalt into the NLM cathodes results in a slight increase in activation energy, leading to a decrease in conductivity. However, the F-containing compounds exhibit
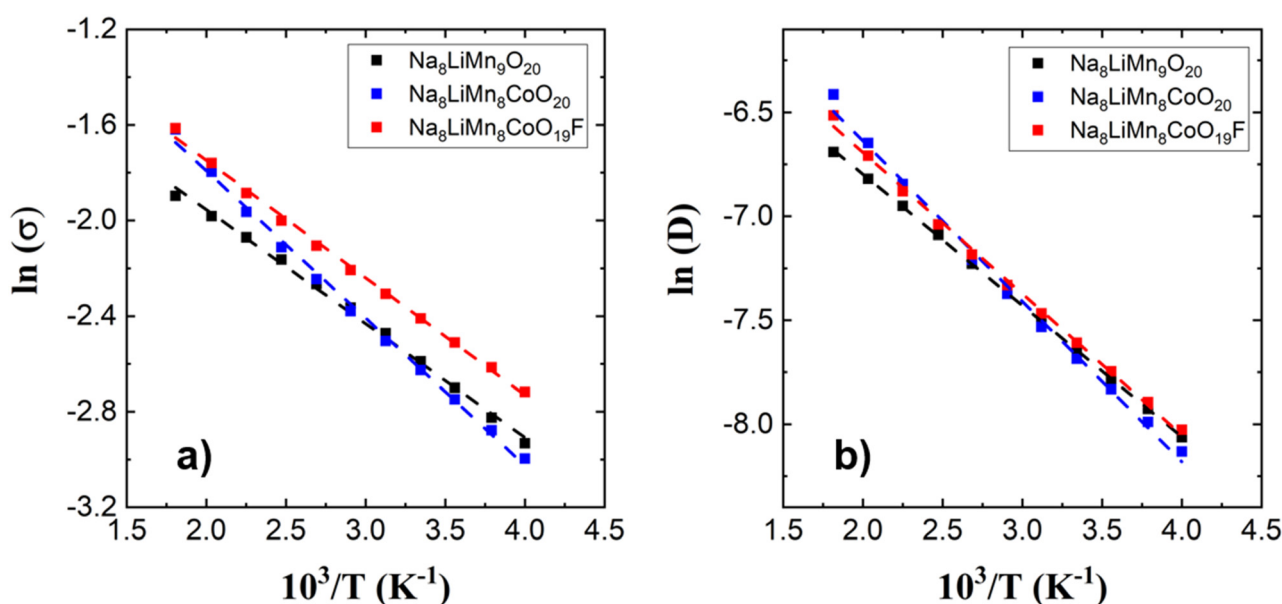

Fig. 6 Arrhenius dependence of (a) conductivity and (b) diffusion coefficient of NLM, Co-doped NLM, and (Co, F) co-doped NLM systems.

Table 3 Activation energy for diffusion (E_a^D) and DC conductivity (E_a^σ), including the conductivity (σ_0) and diffusion coefficient (D_0) at room temperature of NLM, Co-doped NLM, and (Co, F) co-doped NLM systems

Compound	E_a^D (eV)	D_0 ($\times 10^{-8}$ cm^2 s^{-1})	E_a^σ (eV)	σ_0 (mS cm^{-1})
NLM	0.125	1.44	0.095	1.81
Co-doped NLM	0.153	1.21	0.122	1.54
(Co, F) co-doped NLM	0.136	1.50	0.097	2.74

much better transport properties compared to the pristine systems.

The present activation energy and transport properties at room temperature are comparable to those of the cathodes utilized in Na-ion battery technologies. For instance, Aparicio et al.[65] report that the Na$_4$VO(PO$_4$)$_2$ sodium-ion cathode has an activation energy of 0.49 eV and a diffusion coefficient of 5.1 × 10^{-11} cm^2 s^{-1}, respectively. In another study, Aparicio et al.[66] indicate that the NaVOPO$_4$ vanadyl phosphates cathode materials display low Na-ion activation energies of 0.3 eV–0.5 eV and diffusion coefficients at 300 K ranging from 10^{-11} to 10^{-12} cm^2 s^{-1}. In this sense, the compounds considered in the present study, which have relatively low activation energies and room-temperature conductivity ranging from 1.54 to 2.74 mS cm^{-1}, can be regarded as efficient materials for cathodes for current and future SIBs. Moreover, the reduced activation barrier and enhanced Na$^+$ diffusivity of (Co, F) co-doped NLM align with earlier reports in multi-doped layered K-oxides,

where transition-metal disordering creates a larger interlayer spacing and lowers diffusion barriers.[55] Likewise, oxygen-vacancy-assisted co-doping strategies in Li-rich oxides have been shown to boost diffusion coefficients and charge-transfer kinetics.[57] Together, these comparisons highlight that dual cation–anion doping is a universal pathway to accelerate alkali-ion transport.

To further demonstrate the superior performance of the co-doped systems compared to the pristine material, we conduct electrochemical impedance spectroscopy (EIS) to assess their conductivity, electron transport, and diffusivity. The results are shown in Fig. 7 and Table 4. The Nyquist plots (Fig. 7a) for all samples exhibit a distorted semicircle in the high- to medium-frequency range and a straight line in the low-frequency range, indicating a similar overall electrochemical behavior. The equivalent circuit models are obtained by fitting the experimental EIS data with ZView2 software. As shown in Fig. 7c, the equivalent circuit contains three main elements: R_1, representing the ohmic resistance of the system; R_2//CPE$_1$, describing the electrode–electrolyte interfacial processes; and (R_3–W)//CPE$_2$, associated with the electrochemical reaction kinetics.[67] The fitted component values are summarized in Table 4, which reveals a pronounced decrease in system resistance upon doping, following the order: NM > NLM > F doped NLM ≈ Co doped NLM > (Co, F) co-doped NLM. Previous studies have shown that the total system resistance arises from the intrinsic material resistance, the contact resistance between the electrode and current collector, and the electrolyte resistance.[68] Since the electrode preparation and electrolyte composition
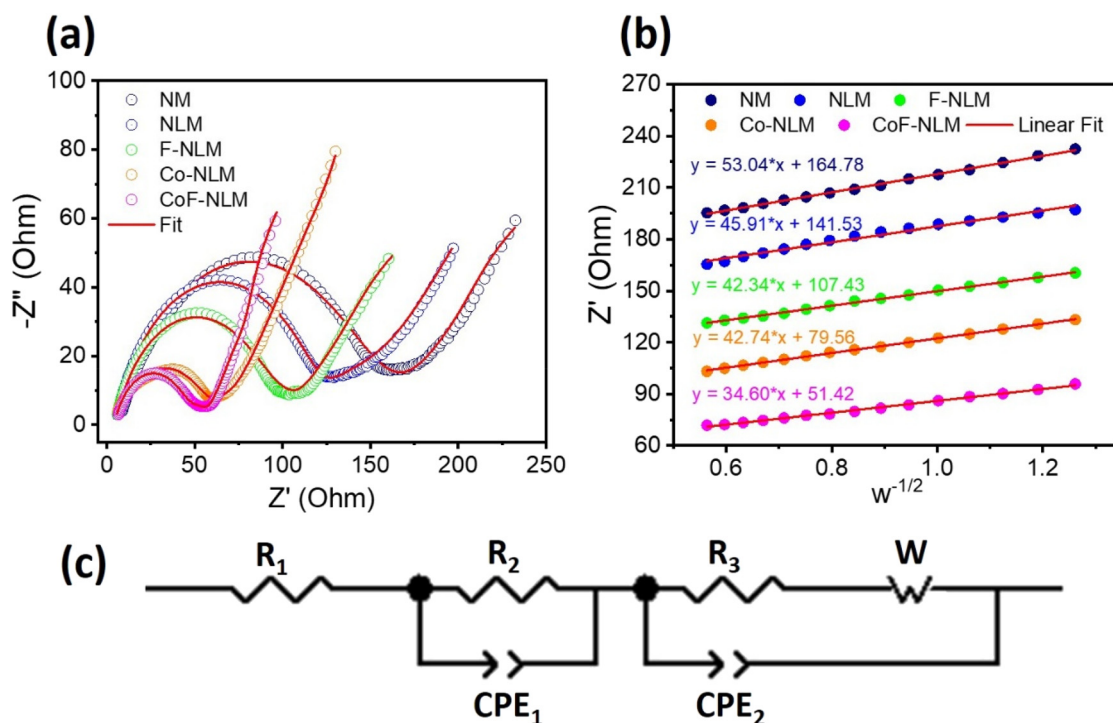
Fig. 7 Nyquist plots (a), $Z'-w^{-1/2}$ plot (b), and equivalent circuit diagram (c).

Table 4 Summary of the electrical component values in the equivalent circuit of the synthesized materials

Samples/elements		NM	NLM	F-NLM	Co-NLM	(Co, F)-NLM
R_1 (Ω)		6.31	4.93	4.69	4.60	4.15
R_2 (Ω)		38.85	30.23	17.22	8.96	8.99
CCPE$_1$	CPE$_{1\text{-T}}$ (F)	1.39×10^{-3}	5.04×10^{-3}	8.18×10^{-3}	3.37×10^{-3}	1.38×10^{-3}
	CPE$_{1\text{-P}}$	0.45	0.59	0.60	0.73	0.72
R_3 (Ω)		123.4	114.4	91.72	55.26	42.95
CCPE$_2$	CPE$_{2\text{-T}}$ (F)	1.07×10^{-5}	8.47×10^{-6}	1.15×10^{-5}	2.36×10^{-5}	1.07×10^{-5}
	CPE$_{2\text{-P}}$	0.76	0.78	0.76	0.67	0.76
W	W_R (Ω)	179.4	346.5	872.9	380.7	148.3
	W_T (F)	9.1	40.42	242.6	13	6.3
	W_P	0.46	0.49	0.51	0.57	0.59

were identical across all samples, the observed reduction in resistance is mainly attributed to lower material resistance in the doped systems. This trend is consistent with the enhanced electronic properties predicted by the DFT calculations.

The diameter of the semicircle reflects two contributions: ion transport across the electrode–electrolyte interface (faradaic resistance, R_2) and charge transport at the electrode surface (charge transfer resistance, R_3). Since the electrode–electrolyte interfacial properties are generally similar across samples, differences in semicircle size are primarily attributed to variations in charge transfer resistance. As shown in Fig. 7a, the smaller semicircles observed for the doped materials, together with the fitted results in Table 4, clearly demonstrate that doping enhances charge transfer by reducing the R_3 value. At low frequency, the Nyquist plots exhibit a straight line, from which the Warburg impedance coefficient (σ) can be obtained by plotting Z' *versus* $\omega^{-0.5}$ according to the equation $Z' = R + \sigma \times \omega^{-0.5}$.[69,70] Fig. 7b shows that σ decreases for all doped systems, with the lowest σ value observed for the (Co, F) co-doped NLM sample, confirming the beneficial effect of (Co, F) co-doping. Previous studies have established that a lower σ corresponds to a higher ion diffusion coefficient.[71] Thus, the reduced σ values further indicate that doping significantly improves ion diffusion kinetics. In summary, the EIS results confirm that doping significantly enhances conductivity, charge transfer, and ion diffusion, enabling the doped materials to deliver superior electrochemical performance, including higher specific capacity, improved rate capability, and enhanced cycling stability.

4. Conclusions

In summary, we have systematically unraveled the underlying mechanisms by which transition-metal and fluorine co-doping govern the stability, electronic conductivity, and ion transport of P2-type sodium–lithium–manganese oxide cathodes. Among all investigated systems, the (Co, F) co-doped configuration emerges as the most promising, showing minimal Jahn–Teller distortion, enlarged unit cell volume, and enhanced long-term stability.

Pristine NLM exhibits ferromagnetic metallic behavior, while (Co, F) co-doping drives a transition to a semi-metallic state with the highest free carrier density and superior conductivity. Charge redistribution, where Li acts as a donor and Co/F as acceptors, further optimizes electronic performance. Transport analyses reveal that (Co, F) co-doping enables low-barrier, one-dimensional Na$^+$ migration pathways within the [MnO$_2$] framework, greatly enhancing ionic mobility.

By integrating advanced first-principles simulations with experimental validation, we identify a cooperative mechanism in which Co suppresses Jahn–Teller distortions and F expands and stabilizes the lattice. This dual action not only explains the superior electrochemical performance of co-doped systems but also provides mechanistic insights inaccessible from experiments alone. These results establish (Co, F) co-doping as a powerful strategy for designing robust, high-performance sodium-ion cathodes, demonstrating the broader potential of dual cation–anion doping in next-generation energy storage materials.

Conflicts of interest

There are no conflicts of interest to declare.

Data availability

All data that support the findings of this study are included in the article and the SI. The Supplementary Information includes structural stability data, synthesis procedures, and electronic property analyses for P2-type sodium lithium manganese oxide batteries co-doped with transition metals and fluorine, as well as sodium-ion diffusion path calculations using BVSE and NEB methods. See DOI: https://doi.org/10.1039/d5dt00638d.

Acknowledgements

References

1 S. Martinet, Nanomaterials for Rechargeable Lithium Batteries, In *Nanomaterials for Sustainable Energy, NanoScience and Technology*, ed. Q. Li, Springer International Publishing, Springer, Cham, 2016, pp. 471–512.

2 N. Yabuuchi, K. Kubota, M. Dahbi and S. Komaba, *Chem. Rev.*, 2014, **114**, 11636–11682.

3 Y. S. Hu, S. Komaba, M. Forsyth, C. Johnson and T. Rojo, *Small Methods*, 2019, **3**, 2–3.

4 J. Xu, D. H. Lee, R. J. Clément, X. Yu, M. Leskes, A. J. Pell, G. Pintacuda, X.-Q. Yang, C. P. Grey and Y. S. Meng, *Chem. Mater.*, 2014, **26**, 1260–1269.

5 C. Delmas, C. Fouassier and P. Hagenmuller, *Physica B+C*, 1980, **99**, 81–85.

6 R. M. Gao, Z. J. Zheng, P. F. Wang, C. Y. Wang, H. Ye and F. F. Cao, *Energy Storage Mater.*, 2020, **30**, 9–26.

7 L. Gao, S. Chen, L. Zhang and X. Yang, *J. Alloys Compd.*, 2019, **782**, 81–88.

8 Á. Caballero, L. Hernán, L. Sánchez, J. Santos-Peña and M. Aranda, *J. Mater. Chem.*, 2002, **12**, 1142–1147.

9 D. Su, C. Wang, H. J. Ahn and G. Wang, *Chem. – Eur. J.*, 2013, **19**, 10884–10889.

10 Z. Zhao, X. Huang, Y. Shao, S. Xu, L. Chen, L. Shi, Q. Yi, C. Shang and D. Zhang, *Chem. Eng. J. Adv.*, 2022, **10**, 100292.

11 Q. Zhao, W. Wang, Y. Li, N. Wu, Y. Guo, W. Cheng, W. Sun, J. Li and A. Zhou, *Electrochim. Acta*, 2021, **390**, 138842.

12 N. V. To, K. V. Nguyen, H. S. Nguyen, S. T. Luong, P. T Doan, T. H. T. Nguyen, Q. Q. Ngo and N. V. Nguyen, *J. Electroanal. Chem.*, 2021, **880**, 114834.

13 A. Sengupta, A. Kumar, A. Bano, A. Ahuja, H. Lohani, S. H. Akella, P. Kumari, M. Noked, D. T. Major and S. Mitra, *Energy Storage Mater.*, 2024, **69**, 103435.

14 W. Wu, P. Zhang, S. Chen, X. Liu, G. Feng, M. Zuo, W. Xing, B. Zhang, W. Fan, H. Zhang, P. Zhang, J. Zhang and W. Xiang, *J. Colloid Interface Sci.*, 2024, **674**, 1–8.

15 L. Wang, Y. You, Z. Li, S. Ou, J. Xu and M. Yuan, *Chem. Eng. J.*, 2025, **506**, 160307.

16 S. Xu, L. Zhao, S. Li and S. Guo, *Chem. Commun.*, 2025, **61**, 4147–4159.

17 M. J. Aragón, P. Lavela, G. Ortiz, R. Alcántara and J. L. Tirado, *J. Alloys Compd.*, 2017, **724**, 465–473.

18 A. W. Zia, S. A. Hussain, S. Rasul, D. Bae and S. Pitchaimuthu, *J. Energy Storage*, 2023, **72**, 108803.

19 Y. Zhao, Y. Li, T. Wang, X. Zhao, X. Kong, G. Li, Z. Wang, F. He, X. Chang, Z. Liu, L. Wu, M. Zhang and P. Yang, *J. Colloid Interface Sci.*, 2025, **677**, 655–664.

20 M. S. Goh, H. Moon, H. Shin, J. Lee, J. S. Lee, N. Park, G. Lee and M. Kang, *Surf. Interfaces*, 2024, **51**, 104721.

21 Q. Deng, Z. Zhao, L. Mao, Y. Zou, B. Gou, Y. Yan, W. Zhang, R. Yang and Y. Xu, *J. Solid State Chem.*, 2023, **328**, 124305.

22 Y. Zhu, X. Tang, Z. You, Y. Zhang, W. Du, Y. Duan, J. Cai and Y. Zhang, *J. Electroanal. Chem.*, 2024, **966**, 118413.

23 Y. Zhang, P. He, J. Zhang, Y. Wen, M. Li, Y. Wang, Z. Zhu and D. Han, *J. Alloys Compd.*, 2023, **965**, 171277.

24 Z. Hossein, T. Du, L. Zhao, S. Zhu, Z. Su, K. Wang, B. Cui, Z. Tan, G. Fan and Z. Li, *Carbon*, 2024, **229**, 119449.

25 T. Jin, P. F. Wang, Q. C. Wang, K. Zhu, T. Deng, J. Zhang, W. Zhang, X. Q. Yang, L. Jiao and C. Wang, *Angew. Chem.,– Int. Ed.*, 2020, **59**, 14511–14516.

26 K. Du, K. S. Ryu and G. Hu, *ECS Electrochem. Lett.*, 2013, **2**, 2013–2015.

27 F. Wei, Q. Zhang, P. Zhang, W. Tian, K. Dai, L. Zhang, J. Mao and G. Shao, *J. Electrochem. Soc.*, 2021, **168**, 050524.

28 A. Konarov, H. J. Kim, N. Voronina, Z. Bakenov and S. T. Myung, *ACS Appl. Mater. Interfaces*, 2019, **11**, 28928–28933.

29 W. Li, Q. Chen, D. Zhang, C. Fang, S. Nian, W. Wang, C. Xu and C. Chang, *Mater. Today Commun.*, 2022, **32**, 103839.

30 M. S. Chae, H. J. Kim, J. Lyoo, R. Attias, Y. Gofer, S.-T. Hong and D. Aurbach, *Adv. Energy Mater.*, 2020, **10**, 2002205.

31 C. Jiang, B. Chen, M. Xu and J. Jiang, *Energy Storage Mater.*, 2024, **70**, 103518.

32 C. J. O. Verzijl and J. M. Thijssen, *J. Phys. Chem. C*, 2012, **116**, 24393–24412.

33 C. Chen and S. P. Ong, *Nat. Comput. Sci.*, 2022, **2**, 718–728.

34 J. P. Perdew, *Phys. Rev. B: Condens. Matter Mater. Phys.*, 1986, **33**, 8822–8824.

35 J. P. Perdew, K. Burke and M. Ernzerhof, *Phys. Rev. Lett.*, 1996, **77**, 3865.

36 H. Sun and K. Zhao, *J. Phys. Chem. C*, 2017, **121**, 6002–6010.

37 J. Wang and X.-Q. Gong, *Appl. Surf. Sci.*, 2018, **428**, 377–384.

38 K. Xiong, Q. Zheng, Z. Cheng and P.-F. Liu, *Eur. Phys. J. B*, 2020, **93**, 201.

39 Z. Hu and H. Metiu, *J. Phys. Chem. C*, 2011, **115**, 5841–5845.

40 C. J. Fennie and K. M. Rabe, *Phys. Rev. Lett.*, 2006, **96**, 205505.

41 M. C. Idris, A. Shaari, R. Razali, A. Lawal and S. T. Ahams, *Comput. Condens. Matter*, 2020, **23**, e00460.

42 J. Gebhardt and C. Elsässer, *J. Phys.: Condens. Matter*, 2023, **35**, 205901.

43 E. Targholi, S. M. Mousavi-Khoshdel, M. Rahmanifara and M. Z. A. Yahya, *Chem. Phys. Lett.*, 2017, **687**, 244–249.

44 K. Harun, N. A. Salleh, B. Deghfel, M. K. Yaakob and A. A. Mohamad, *Results Phys.*, 2020, **16**, 102829.

45 G. Kresse and J. Furthmüller, *Comput. Mater. Sci.*, 1996, **6**, 15–50.

46 G. Kresse and J. Hafner, *Phys. Rev. B: Condens. Matter Mater. Phys.*, 1994, **49**, 14251–14269.

47 H. J. Monkhorst and J. D. Pack, *Phys. Rev. B*, 1976, **13**, 5188–5192.

48 Y. Wang, Z. Feng, P. Cui, W. Zhu, Y. Gong, M.-A. Girard, G. Lajoie, J. Trottier, Q. Zhang, L. Gu, Y. Wang, W. Zuo, Y. Yang, J. B. Goodenough and K. Zaghib, *Nat. Commun.*, 2021, **12**, 13.

49 H. Kim, K. Kim and S. Kim, *J. Phys. Chem. Lett.*, 2024, **15**, 1347–1354.

50 X. Chen, G. Lin, P. Liu, Z. Sun, Y. Si, Q. Wang and L. Jiao, *Energy Storage Mater.*, 2024, **67**, 103303.

51 H. H. Sun, H. H. Ryu, U. H. Kim, J. A. Weeks, A. Heller, Y. K. Sun and C. B. Mullins, *ACS Energy Lett.*, 2020, **5**, 1136–1146.

52 T. H. N. Thi, N. T. Van, M. T. Dang, N. V. A. Duy, T. S. Luong, S. D. Le, T. N. Van, D. L. Vu and N. N. Van, *J. Electroanal. Chem.*, 2024, **972**, 118590.

53 E. Gonzalo, M. Zarrabeitia, N. E. Drewett, J. M. López del Amo and T. Rojo, *Energy Storage Mater.*, 2021, **34**, 682–707.

54 N. Ortiz-Vitoriano, N. E. Drewett, E. Gonzalo and T. Rojo, *Energy Environ. Sci.*, 2017, **10**, 1051–1074.

55 X. Ding, Y. Wang, X. Wang, L. Geng, C. Guo, W. Liu, H. Wang, C. Sun and C. Han, *Chem. Eng. J.*, 2023, **466**, 143331.

56 F. Wang, P. Zuo, Z. Xue, Y. Liu, C. Wang and G. Chen, *ACS Energy Lett.*, 2024, **9**, 1249–1260.

57 H. Zhang, J. Dong, G. Chen, H. Che, K. Yan, X. Wang, J. Liu, D. Liu, Y. Lu, N. Li, Y. Su, F. Wu and L. Chen, *Chem. Eng. J.*, 2025, **506**, 159902.

58 A. Langella, A. Massaro, A. B. Muñoz-García and M. Pavone, *Chem. Mater.*, 2024, **36**, 2370–2379.

59 Y. Li, Y. Mei, R. Momen, B. Song, Y. Huang, X. Zhong, H. Ding, W. Deng, G. Zou, H. Hou and X. Ji, *Chem. Sci.*, 2024, **15**, 349–363.

60 Z. Zheng, J. Zhou and Y. Zhu, *Chem. Soc. Rev.*, 2024, **53**, 3134–3166.

61 A. H. Al-Marri, *J. Solid State Electrochem.*, 2024, **28**, 2861–2872.

62 Y. A. Zulueta and M. T. Nguyen, in *Annual Reports in Computational Chemistry*, Elsevier, 2023, vol. 19, pp. 1–43.

63 Y. A. Zulueta and M. T. Nguyen, *Phys. Chem. Chem. Phys.*, 2023, **25**, 27926–27935.

64 S. Zhang, J. Ma, S. Dong and G. Cui, *Electrochem. Energy Rev.*, 2023, **6**, 4.

65 P. A. Aparicio and N. H. de Leeuw, *Phys. Chem. Chem. Phys.*, 2020, **22**, 6653–6659.

66 P. A. Aparicio, J. A. Dawson, M. S. Islam and N. H. de Leeuw, *J. Phys. Chem. C*, 2018, **122**, 25829–25836.

67 W. Wang, S. Guo, I. Lee, K. Ahmed, J. Zhong, Z. Favors, F. Zaera, M. Ozkan and C. S. Ozkan, *Sci. Rep.*, 2014, **4**, 4452.

68 H. Nara, D. Mukoyama, R. Shimizu, T. Momma and T. Osaka, *J. Power Sources*, 2019, **409**, 139–147.

69 T. H. N. Thi, N. T. Van, M. T. Dang, N. V. A. Duy, T. S. Luong, S. D. Le, T. N. Van, D. L. Vu and N. N. Van, *J. Electroanal. Chem.*, 2024, **972**, 118590.

70 A. A. Moya, *J. Energy Storage*, 2024, **97**, 112911.

71 T. Q. Nguyen and C. Breitkopf, *J. Electrochem. Soc.*, 2018, **165**, E826.